Assessment of microvasculature flow state with a high speed all-optic dual-modal system of optical coherence tomography and photoacoustic imaging

ZHENHE MA,[1,*] SHUZHUO LUO,[2] MENGHAN YU,[1] JIAN LIU,[1] YUQIAN ZHAO,[1] YAO YU,[1] JIANGTAO LV,[1] XIAOFANG ZHANG,[3] AND YI WANG[1]

[1]School of Control Engineering, Northeastern University at Qinhuangdao, Qinhuangdao 066004, China
[2]School of Computer Science and Engineering, Northeastern University, Shenyang 110004, China
[3]School of Optoelectronics, Beijing Institute of Technology, Beijing 100081, China
*mazhenhe@163.com

Abstract: We propose a high speed all-optic dual-modal system that combines spectral domain optical coherence tomography (SDOCT) and photoacoustic imaging (PAI) to evaluate microvasculature flow states. A homodyne interferometer was used to remotely detect the surface vibration caused by photoacoustic (PA) waves. The PA excitation, PA probing and SDOCT probing beams share the same X-Y galvanometer scanner to perform fast two-dimensional scanning. In addition, we introduced multi-excitation, dual-channel acquisition and sensitivity compensation to improve the imaging speed of the PAI sub-system. The total time for imaging a sample with 256 × 256 pixels is less than 1 minute. The performance of the proposed system was verified by *in vivo* imaging of the vascular system in a mouse pinna with normal and then blocked blood circulations. The experimental results indicate that the proposed system is capable of revealing different blood flow states (static and moving) and is useful for the study of diseases related to functional blood supply.

1. Introduction

Mammalian cells require oxygen and nutrients to survive, and therefore locate within 100 to 200μm distance from the blood vessels — the diffusion limit for oxygen [1]. The vascular system regulates blood flow and tissue perfusion which is essential for organ function [2]. Many diseases originate or associate with vascular system disorders [1,3–5]. Visualization of blood vessel distribution and differentiation of the flow state in vessels are important for the diagnosis and pathogenesis analysis of vascular diseases [6–9].

Many technologies have been developed to image blood vessels, namely angiography. Magnetic resonance imaging (MRI), computed tomography (CT), positron emission tomography (PET), ultrasonography and digital subtract angiography (DSA) have proven to be effective in visualizing large vessels. However, these methods are unlikely to be efficacious for observing small vessels because of their comparatively lower resolution [8–10]. Fluorescence microscopy and multiphoton microscopy have sufficient spatial resolutions for imaging capillaries, but they are invasive imaging modalities requiring agent injection into samples. Optical coherence tomography (OCT) provides depth-resolved images in turbid media with high spatial and temporal resolutions [11]. OCT angiography (OCTA) was first proposed in 2007 as a functional extension to OCT technique [12]. OCTA can provide non-invasive, non-contact, three-dimensional blood flow perfusion images based on backscattering properties from moving particles such as red blood cells. It has been successfully employed to obtain detailed micro-capillary networks in different biological tissues *in vivo*, such as the retina, skin, brain and skeletal muscle [7,8,13,14]. Photoacoustic imaging (PAI) is also a non-invasive imaging modality feasible for structural, functional, and molecular imaging [15].

PAI detects ultrasonic signals produced by light absorption in a sample. Due to the high light absorption characteristic of hemoglobin, PAI is sensitive to all blood vessels regardless of flowing states inside. Both OCTA and PAI are powerful tools for angiography, and their combination can provide more useful information of blood flow for the vascular diseases, such as stroke.

In recent years, some multi-modal imaging systems combining PAI and OCT have been reported [16–21]. The integration of the two modalities is limited by the discrepancy of their detection components. The transducer used in PAI obstructs OCT scanning [22]. Optical interferometric methods, such as Mach–Zehnder interferometer [23–25] and Fabry–Perot interferometer [26–28], have been proposed as the alternatives to transducers. These techniques also have difficulties for the combination with OCT, because bulky and complicated optics are involved in general [29]. Fiber based Michelson interferometers have been reported for photoacoustic (PA) signal detection, including low-coherence and long-coherence interferometers [30,31]. Park et al. proposed an all-fiber heterodyne interferometer for non-contact PA tomography (PAT) [32]. Using this technique, Eom et al. established an all-fiber-optic PAT and OCT multi-modal system. In order to achieve heterodyne detection, acousto-optic modulation is required and the reported system is complex. The homodyne interferometer is relatively simple and easy to be implemented [31,33]. However, the sensitivity of the system varies due to ambient disturbance. Data acquisition is recommended to be performed when the system reaches its maximum sensitivity. This operation is time consuming and reduces the imaging speed of the multi-modal system.

In this paper, we present a high speed, all-optic dual-modal system that integrates OCT and PAI. To improve the imaging speed of PAI, a novel acquisition strategy was adopted, including multi-excitation, reference arm modulation, and 2-channel acquisition. It is unnecessary to lock the system at its maximum sensitivity. PA signals were compensated according to the instantaneous systematic sensitivity. To test the capability of the system for assessing blood flow state, the vasculatures of a mouse pinna was imaged *in vivo* with and without flowing blood.

2. System and method

2.1 OCT and PAI dual-modal system

The dual-modal setup used in this study integrated a spectral domain OCT (SDOCT) subsystem and a PAI subsystem with optical detection as illustrated in Fig. 1. In the SDOCT subsystem, we use a broadband infrared superluminescent diode (SLD, D-840-HP, Superlum) with a central wavelength of 840 nm and a full width at half maximum (FWHM) bandwidth of 80 nm as the illumination source to provide an axial resolution of ~6 μm in air (red beam in Fig. 1). The ex-fiber output power was rated at ~15 mW. Light from SLD went through an optical circulator and was split into a probing arm and reference arm through a 2 × 2 fiber coupler with 10:90 split ratio. The ninety percent power path went to the probing arm while the ten percent power path went to the reference mirror. The lights reflected back from both reference and probing arms met and interfered with each other at the fiber coupler, and the resulting interferogram was sent via the optical circulator to a custom-built high-speed spectrometer. The spectrometer consists of a transmission grating (1800 lines/mm), a camera lens with a focal length of 100 mm, and a line-scan camera (spL2048-140km, Basler). The theoretical depth range was calculated to be ~2.4 mm in air. The line-scan camera was running at 50,000 Hz to convert interferograms to digital signals. With each B-scan frame (i.e. X direction) containing 256 A-lines, the imaging speed of the OCT can reach 160 frames per second. The space between adjacent A-lines is ~5 μm and each B-scan spans is ~1.3 mm. The C-scan consists of 256 cross-sections with ~5 μm space interval covering ~1.3 mm. The acquired interferogram data were transmitted to a workstation through an image grabber (PCIe-1433, NI).
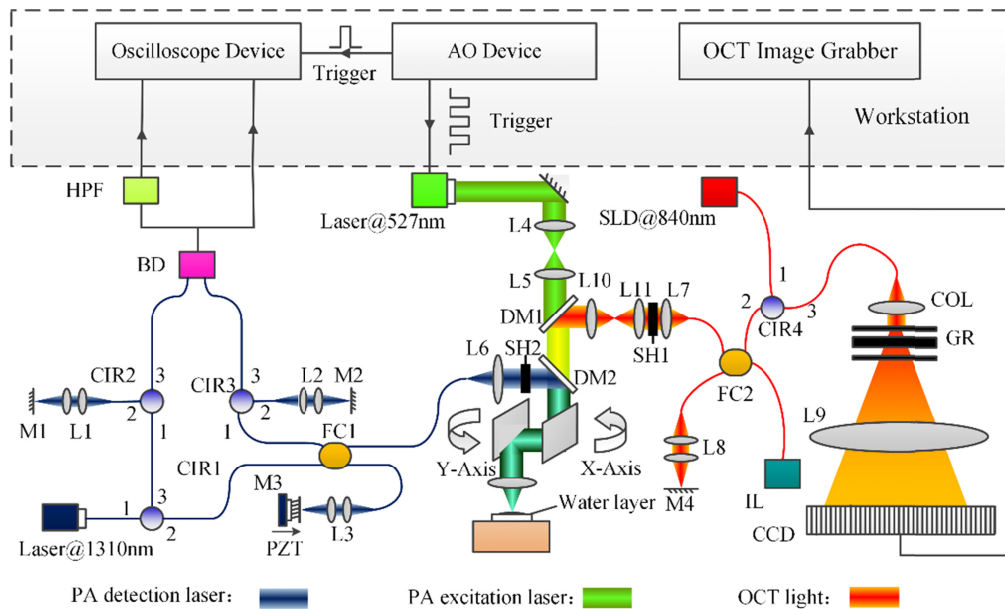
Fig. 1. Schematic of the experimental setup. HPF: High-pass Filter, BD: Balanced Detector, PZT: Piezo-translator, CIR: Circulator, M: Mirror, L: Lens, FC: Fiber Coupler, IL: Indicator Light, COL: Collimator, DM: Dichroic Mirror, SLD: Superluminescent Diode, SH: Shutter.

In the PAI subsystem, photoacoustic signals were excited by a laser with a wavelength of 527 nm and a pulse duration of 7 ns (green beam in Fig. 1). Ultrasonic waves generated by the light absorption propagated to the sample surface and were detected by a fiber based Michelson interferometer working at 1310 nm (blue beam in Fig. 1). The light source of the interferometer is a laser diode with a bandwidth of 0.1nm (LSDLD131-4-S-0-1-bSMFA, Beijing lightsensing Technologies Ltd). The reference mirror (M3 in Fig. 1) was mounted on a piezo-translator (PZT, P-620.1CD, PI) to change the optical path length of the reference arm. The PZT was controlled by an analog output (AO) device (PCI-6713, NI). In order to increase the intensity of the probing beam reflected back from the surface of a sample, the sample was covered with a thin layer of water. The interference signals were delivered to a balanced detector (BD, PDB465C, Thorlabs). The two circulators provided an additional light intensity adjustment by mirror reflection (CIR2, M1; CIR3, M2 in Fig. 1). A high speed oscilloscope device (PCI-5124, NI) with two channels was used for signal digitalization. One channel acquired the BD output signal for the later PA sensitivity compensation, while the other channel acquired high-pass filtered BD output for PA signal extraction. The excitation laser and the oscilloscope device were triggered by a pulse chain generated by a counter port of the AO device. During signal acquisition, the AO device drove the PZT to modulate the interference phase. The bandwidth of the PAI subsystem is about 40 MHz.

For the dual-modal system, three beams illuminated on the sample, including the OCT probing, PAI probing, and PAI excitation beams. These beams were combined by two dichroic mirrors, and were delivered onto the sample through an optical probing arm that contains an X-Y scanner and an objective lens (~50 mm focal length). Sharing the same X-Y scanner, the PAI has a scanning protocol similar to OCT, i.e. 256×256 ($X \times Y$) matrix to cover the 1.3×1.3 mm^2 area of the sample. The scanner was controlled by the AO device to perform a 2D scanning on the sample for excitation and detections. The objective lens focused lights on the sample. The lateral resolution of the system is measured to be ~8 μm for OCT and ~11 μm for PAI. There are two shutters in OCT and PAI probing arms as shown in Fig. 1 (SH1 and SH2). During data acquisition, only one shutter is opened to avoid incident lights superimposing.

2.2 OCT angiography

The detailed description of OCTA has been described previously [34,35]. In SDOCT, the interferogram is captured by the line-scan camera. For simplicity, we ignore all components that do not contribute to the useful information about microstructure and flow. The interferogram can be expressed as:

$$I(t,k) = 2S(k)E_R \int_{-\infty}^{\infty} a(z,\ t)\cos[2kn(z-\ vt)]dz, \tag{1}$$

where k is the wavenumber; t is the time at which the interferogram is captured; E_R is the amplitude of the light reflected from the reference mirror; $S(k)$ is the spectral density of the light source; z is the depth; $a(z,\ t)$ is the amplitude of the light backscattered from the sample; n is the refractive index; v is the axial velocity of blood cells. According to previous analysis [36,37], the sensitivity to the flow velocity detection is determined by the time interval between adjacent interferograms used for velocity calculation. The sensitivity increases with the time interval elongating. Here, high-pass filtering was applied along the slow scanning C-scan direction to isolate the scattering signal from moving blood cells from the static tissue. Since two B-scans were acquired in each cross-section along the C-scan direction with Δt_B time interval, a differential operation was applied to the subsequent B-scan at each cross-section. This can be described by the following equation:

$$I_j(t,k) = I(t,k) - I(t + \Delta t_B, k), \quad j = 1, 2, 3...256, \tag{2}$$

where $I_j(t,k)$ denotes the flow signal at jth cross-section (total of 256 cross-sections) along the C-scan direction. As the differential operation is equivalent to high-pass filtering, it suppresses optical scattering signals from static elements. Then, by applying fast Fourier transforms (FFT) upon every wavenumber k of $I_j(t,k)$, we can obtain a depth-resolved flow image sensitive to blood flow for each cross section. With all the cross-sectional flow images, 3D volumetric perfusion map can be rendered using visualization software.

2.3 High speed PAI with multi-excitation and sensitivity compensation

In our PAI subsystem, the sample was illuminated by a focused short pulse laser. The absorption of laser energy by local absorbers inside a sample generated ultrasonic waves via thermal-elastic expansion. With plane-wave approximation, the ultrasonic waves leading surface vibration are expressed as [38]:

$$p(t) = \frac{C}{2}\frac{\partial \varepsilon(t)}{\partial t}, \tag{3}$$

where $p(t)$ is the pressure of the ultrasonic wave, $\varepsilon(t)$ is the surface displacement, and C is the acoustic impedance of the medium. Note that the scaling factor half represents the free boundary condition at the air–tissue interface. A fiber based homodyne interferometer was used to measure the surface displacement. In order to eliminate the DC component of the interference signal, balance detection was performed. Therefore, the intensity of the signal can be described as [39]:

$$D(t) = A\cos[\phi(t) + \frac{4\pi}{\lambda}\varepsilon(t)], \tag{4}$$

where the coefficient A is related to the intensities of the two interfering beams; λ is the wavelength of the detection laser; $\phi(t)$ is the optical phase difference between the probing and reference beams related to variations in ambient conditions. $\phi(t)$ varies slowly (less than a few hundred Hz). The surface vibration ($\varepsilon(t)$) resulted from PA pressure possess frequency

components much higher than $\phi(t)$. In order to study the frequency content of the interference signal, Eq. (4) may be expanded to a harmonic series with amplitudes given by Bessel functions of the first kind [40]. For the detection principle presented here, it is sufficient to consider only the two lowest order components of the series expansion. Equation (4) can be further approximated as:

$$D(t) = A\cos\phi(t) + \frac{4\pi A}{\lambda}\sin\phi(t)\cdot\varepsilon(t). \qquad (5)$$

The second term of Eq. (5) is the PA signal modulated by phase. Figure 2(a) shows a typical digitalized interference signal using a tungsten filament as the sample, including eight PA waves (PA_{1-8}). We applied high-pass filtering to eliminate the low frequency component in Eq. (5) and obtained:

$$DHF(t) = \frac{4\pi A}{\lambda}\sin\phi(t)\cdot\varepsilon(t). \qquad (6)$$

Equation (6) shows that the sensitivity of the PAI system is determined by the term $\sin\phi(t)$ [41]. The value $\phi(t) = (2n-1)\pi/2$ having an integer n corresponds to the so-called quadrature points (QPs), where the sensitivity is maximum. Figure 2(b) shows the high-pass filtered result corresponding to the signal in (a). The two signals were acquired simultaneously with a 2-channel oscilloscope card. Though PA signals were excited at the same point of the sample, the extracted amplitudes varied with the interference phase. The amplitudes of PA_1 and PA_3 were relatively larger than other PA signals because the former two signals were acquired when $\phi(t)$ was close to the QPs. In the reported interferometer based PAI system, PA signals were excited and acquired when $\phi(t)$ met this requirement [31]. This operation obviously reduces the scanning speed since the changes of interference phase ($\phi(t)$) are unpredictable.
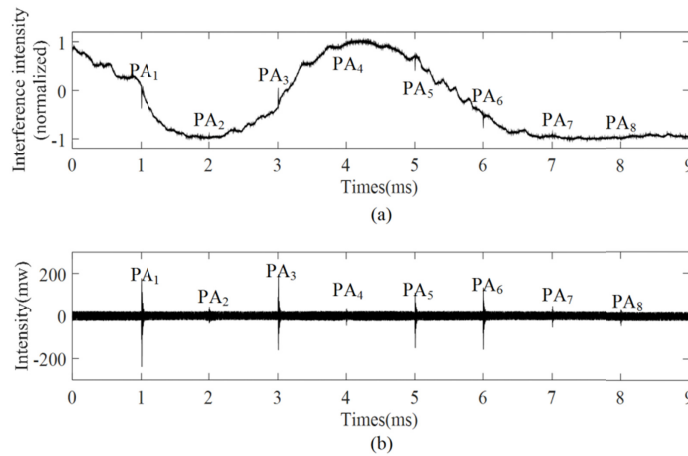

Fig. 2. PA wave extraction with high-pass filtering. (a) Measured interference signal with PA waves. (b) Measured high-pass filtered result of signal in (a). PA_{1-8}: PA waves.

In Fig. 2(b), PA waves are easy to be recognized (PA_{1-8}). Therefore, it is possible to determine the time point (t_p) just before the PA wave reaches the surface. Since $\varepsilon(t)$ is zero at time t_p (Eq. (5)), we can calculate the interference phase:

$$\phi(t_p) = \arccos(\frac{D(t_p)}{A}),\tag{7}$$

where A is the amplitude of *D(t)*. Hence, surface displacement caused by PA waves can be achieved as follows:

$$\varepsilon(t) = \frac{\lambda \cdot DHF(t)}{4\pi A \cdot \sin\phi(t_p)}.\tag{8}$$

The calculated $\varepsilon(t)$ is used to reconstruct PAI images. The advantage is that the varying sensitivity is compensated. This provides the potential for improving the scan speed. In Eq. (8), when $\phi(t)$ is close to $n\pi$, the sensitivity is approximately zero (PA$_{2,4,7,8}$ in Fig. 2). In such a case, sensitivity compensation is susceptible to system noise; therefore data acquired within those regions need to be exempted from image reconstruction. To avoid such influence, three pulses were generated by counter port of AO device (Fig. 1) at each scanning point on the sample. The pulses were used to trigger the excitation laser source and data acquisition. The output of the balance detector ($D(t)$) and its high-pass filtered signal ($DHF(t)$) are simultaneously acquired by the 2-channel oscilloscope card. During acquisition, the reference mirror was modulated by the PZT. The moving speed of the PZT was controlled in accordance with the excitation pulse frequency. This ensures that at least one of the three PA signals is not measured at regions where $\sin\phi(t)$ is close to zero (detailed description is shown in section 3.1).

3. Experimental results

3.1 PAI sensitivity compensation

In order to evaluate the proposed high speed PA imaging method, we imaged a phantom with a fine tungsten filament (~100 μm) embedded in scattering gel. Focusing on the same position on the tungsten filament, PA signals were excited with three sequential laser pulses (~5 kHz frequency). Figure 3(a) shows three BD output waveforms acquired without a reference arm modulation. The excitations were completed in ~0.5 ms, and the interference phase ($\phi(t)$) of two waveforms changed little during such a short period of time (red and pink lines in Fig. 3(a)). Therefore, three PA waves may all fall into the low sensitivity region, which will affect the accuracy of the sensitivity compensation. This problem can be solved by reference arm modulation. During the acquisition, the reference mirror was controlled to shift ~330 nm ($\lambda / 4$), which introduced a π phase change. Therefore, at least one PA wave can be free from the low sensitivity regions (PA$_1$ and PA$_3$ in Fig. 3(b)). The high-pass filtered signal acquired by the other channel is shown in Fig. 3(c). Then, the three PA signals were compensated using the proposed methods, where $\phi(t) = 81.6°, 9.4°, \text{and} 68.8°$ respectively (Fig. 3(d)). We can see that the amplitudes of PA$_1$ and PA$_3$ are similar. The signal of PA$_2$ was over-compensated because it falls into the low sensitivity region and $\sin\phi(t)$ approximates zero. To evaluate the effect of the reference arm modulation, the phantom was imaged without and with modulation, and the sensitivity compensated images were shown in Fig. 3(e) and 3(f), respectively. We can see that the intensity of tungsten filament is not uniform in the image (Fig. 3(e)). This means that under-compensation or over-compensation may occur in the low sensitivity region. The proposed method utilized reference arm modulation and high sensitivity region signal selection, and achieved a better imaging result (Fig. 3(f)).

Traditionally, PA signals need to be acquired at QPs for a homodyne interferometer based vibration measurement. The advantage of this operation is that the maximum sensitivity can be

achieved for each measurement. However, this operation limits the imaging speed. The occurrence of QPs depends on the slowly changing ambient conditions. For a 256 × 256 (X × Y) matrix PAI scanning, the total time varies from 15 to 30 minutes depending on the occurrence frequency of QPs. This time is much longer than OCTA (~5 seconds) and the overall imaging speed of the dual-modal system is slowed down. In the proposed method, the scanning speed is controlled by the program and the acquisition time is constant at each position(~0.5 ms). Therefore, the total scan time of the same matrix is ~40 seconds which is much closer to that of OCTA. Consequently, the total imaging time of the non-contact dual-modal system is less than 1 minute, which makes it possible to monitor changes in blood flow in short time intervals. The proposed method detects PA signal with a slightly lower sensitivity than the conventional maximum sensitivity locking detection. This can decrease the amplitude of the PA signal originally acquired ($DHF(t)$). Considering the noise level of the system is constant, the signal to noise ratio (SNR) of the proposed method decreases. The average SNR measured in Fig. 4(f) is 36 dB, which is lower than the sensitivity locking detection (39 dB).
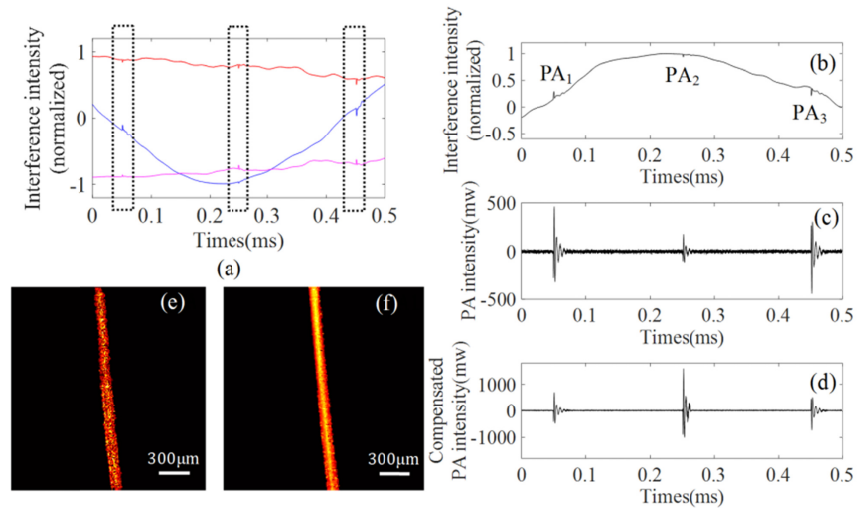

Fig. 3. PA signal sensitivity compensation with reference arm modulation. (a) Multi-excitation PA signals without reference arm modulation. (b) Multi-excitation PA signals with reference arm modulation. (c) High-pass filtered result of waveform in (b). (d) Sensitivity compensated PA signals. (e) PA image of tungsten filament acquired without reference modulation. (f) PA image of tungsten filament acquired with reference arm modulation.

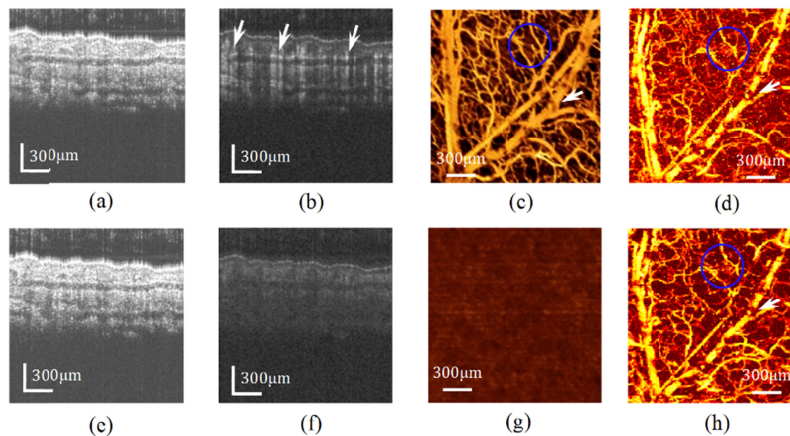## 3.2 Dual-modal imaging to differentiate blood flow states

Fig. 4. Differentiation of blood flow states with dual-modal system. (a,e) OCT cross-sectional structural images of mouse pinna. (b,f) Blood flow images extracted by OCTA algorithm. (c,g) *En face* microvasculature image of OCTA. (d,h) PA images of mouse pinna. (a,b,c,d): images with normal blood flow. (e,f,g,h):images with blood flow blocking.

To demonstrate the imaging capability of the proposed system, we imaged the microvasculature in a mouse pinna *in vivo*. An eight-week-old mouse (female) was anesthetized with 2% isoflurane (0.2 L/min O2, 0.8 L/min air). The mouse pinna was depilated with a commercial human hair remover lotion. The treated mouse pinna was then flatly affixed to a glass block and imaged with the dual-modal system (Fig. 4(a)-4(d)). Then, the blood flow in the imaging region was blocked using bulldog clamp and the imaging results were shown in Fig. 4(e)-4(h). A thin layer of water covered the mouse's pinna to reduce the influence of surface roughness during PA imaging. However, water coverage can introduce strong specular reflection on the surface of the water film, which can cause OCT interferogram to saturate and deteriorate image quality. Furthermore, water coverage can slow the blood circulation in mouse pinna and decrease the quantity of visible blood vessels in OCTA. For each dual-modal imaging, the OCTA scan is prior to PAI in sequence. After OCT imaging, water droplets were placed on the mouse's pinna to create a water film. All experiments were performed in accordance with the National Institutes of Health Guide for the Care and Use of Laboratory Animals and the Animal Ethical Committee of Northeastern University. The incident light power on the sample during OCTA imaging is ~3 mW. For PAI subsystem, the transient fluence of the excitation laser is 16mJ/cm^2, and the power of probing beam is ~3 mW.

Figure 4(a) and 4(e) show typical OCT B-scan cross-sectional structure images captured with and without flowing blood, respectively. We can see that there is no obvious structural change between the two images. The OCTA algorithm was performed to extract blood flow information, and the results are shown in Fig. 4(b) and 4(f). Vessels with flowing blood are highlighted successfully (white arrows in Fig. 4(b)). After blood flow blocking, there is no highlighted information in Fig. 4(f). *En face* OCTA images are presented in Fig. 4(c) and 4(g) by combining all of the flow images. Obviously, the microvasculature distribution of the mouse pinna cannot be extracted by OCTA after blood flow blocking (Fig. 4(g)). The corresponding PAI results are shown in Fig. 4(d) and 4(h). These two images are similar because PAI is independent of the blood flow state. The combination of information from OCTA and PAI makes it possible to distinguish blood flow status. According to Fig. 4(c) and 4(d), we can determine that the blood in the mouse pinna was flowing at the time, because blood vessels were visualized by both the techniques. This is consistent with the experiment because Fig. 4(c) and 4(d) were acquired with normal blood flow. After flow blocking, the blood vessels are not

visible by the OCTA technique (Fig. 4(g)), although vasculature was still present in the mouse pinna (Fig. 4(h)). The dual-modal system may be applied to stroke research. Ischemic stroke is caused by a block of blood supply, for example, a thrombus that occludes the artery. For OCTA technique, two acquisitions (before and after occlusion) are required to determine the occluded parts of the blood vessels. The proposed system can use a single dual-modal scan to distinguish the flow state in blood vessels without having to compare it with previous results. OCTA is a motion sensitive technique; therefore it is unable to visualize some capillaries with very small flow velocity (blue circle in Fig. 4(c)). However, these vessels can be seen in PAI due to the presence of red blood cells and corresponding light absorption (blue circles in Fig. 4(d) and 4(h)). This result indicates that OCTA and PAI are complementary. Comparing the OCTA and PAI images, we can see that the diameters of the blood vessels in OCTA are larger than in PAI, especially in big vessels. This may be attribute to that OCTA can extract the entire flow area of the blood vessel from the cross-sectional scan images, while PAI only visualize red blood cells distributed in the center of the vessel for normal blood flow (axial flow) and sedimentate at the bottom when the flow stops. There are some low intensity speckles in our angiography images, and their positions correspond in OCTA and PAI (white arrows in Fig. 4(c),4(d),4(h)). The cause of speckles is unclear and should be uncovered in future research.

4. Discussion

To achieve non-invasive vasculature imaging using endogenous contrast, optical imaging could be an option. Scattering and absorption are two categories of light–tissue interaction, represented by OCTA and PAI, respectively. Based on the backscattered light from the sample, OCTA can extract intrinsic motion signal introduced by flowing blood cells from the surrounding static tissue. Thus, OCTA is able to visualize vessels with flowing blood, which represents blood flow perfusion (functional blood vessels). Most severe pathologies are associated with vascular abnormalities, such as stroke, trauma and cancer. Mapping blood flow perfusion is help to the pathogenesis of these diseases. With the progress of these diseases, another mechanism is activated and the damaged or blocked blood vessels begin to necrotize and are absorbed by surrounding tissue. However, because blood cells in these vessels don't move any more, OCTA cannot catch these vessels and monitor their progress. On the other hand, PAI can display all blood vessels with hemoglobin presence. The combination of OCTA and PAI is able to distinguish flow conditions in blood vessels, which makes it possible to monitor the entire process of disease development. The proposed dual-modal system integrates two complementary imaging techniques and can provide both anatomic and functional vasculatures.

In our proposed system, the two detection units are all fiber based interferometers that bear the advantages of simplicity, compactness and flexibility. Although the PAI excitation part is still in free space, the high power laser was combined with the other two detection beams before the X-Y scanner. Therefore, the scanning part of the dual-modal system is compact and easy to operate. Two dichroic mirrors were used for combining three light beams, namely the OCT probing beam (~840 nm), the PA excitation laser beam (527 nm) and the PA signal detection beam (1310 nm). Dichroic mirrors provide high coupling efficiency for beams with different wavelength (>90%). However, the dichroic mirror introduces additional dispersion to the sampling arm of OCT subsystem and causes dispersion mismatch between the two interference arms, which degrades the axial resolution of the OCT. Using the dispersion compensation algorithm [42], the resolution reduction was partially compensated. The measured axial resolution is ~8 μm in air slightly lower than the theoretical value ~6 μm. Considering that the refractive index of the sample is ~1.35, this axial resolution is sufficient for imaging the capillary (7~8 μm).

The PAI subsystem uses fine optical focusing to provide lateral resolution, while the axial resolution is still derived from time-resolved ultrasonic detection, which is called optical resolution photoacoustic microscopy (OR-PAM) [43]. However, focusing the excitation laser

beam restricts the imaging depth to the transport mean-free path (TMFP) [44]. The TMFP is the depth at which photon scattering directions become randomized and limits the penetration of ballistic optically focused microscopy systems (including OCT and PAM). In soft tissue, the TMFPs of the OCT and PAI are calculated as [45,46]: $l_t(\lambda_{PA} = 527\,nm) = 0.57\,mm$ and $l_t(\lambda_{OCT} = 840\,nm) = 1.03\,mm$, respectively. This means that the OCT has a deeper penetration depth than the PAI. On the other hand, the SNR of the OCT subsystem is measured to be 96 dB, while PAI is only 36 dB. The relatively low SNR decreases the contrast of deep blood vessels in PAI image, and thus deteriorates the penetration depth. We can see that some small deep vessels in Fig. 4(d) have low contrast and are difficult to distinguish, while the blood vessels in Fig. 4(c) are clear and have high contrast. Increasing the power of the excitation laser or optimizing the detection sensitivity can improve the penetration depth of PAI [47].

Because shutters are used to avoid incident light superimposing between OCT and PAI, their safety limits of American National Standards Institute (ANSI) should be considered separately. For PAI, the imaging area is 1.3×1.3 mm^2, and the power of the detection beam is 3 mW, so its average surface power is 0.18 W/cm^2, which is much lower than the average power limit of 3 W/cm^2 set by the ANSI. The transient fluence of the excitation laser is 16 mJ/cm^2, which is lower than the single pulse limit set by ANSI of 20 mJ/cm^2. For multi-excitation situations, the maximum permissible exposure (MPE) for each single pulse within the group shall not exceed the single-pulse MPE limit multiplied by a correction factor of $n^{-0.25}$, where n is the number of pulses [48]. With three laser pulse excitation at each point, the equivalent transient fluence limit is 15.2 mJ/cm^2, which is close to that we used in this study. Therefore, the total incident power on the sample is slightly higher than ANSI limit in PAI subsystem. For OCT, its incident power is the same as that of the probing beam in PAI, which is lower than the ANSI limit.

Non-contact optical detection of ultrasound in biological tissues is of great interest because it expands the scope of PAI to biomedical applications where contact is impractical [49]. Heterodyne interferometer based method uses an acousto-optic modulator (AOM) to frequency-modulate the reference beam. The interference signal is demodulated using an in-phase and quadrature demodulator. The two demodulated signals are captured for image reconstruction [50]. Heterodyne interferometer is relatively less sensitive to ambient noise compared with the homodyne one and does not need active stabilization [32]. However, the detection sensitivity defined as the peak value divided by the noise root-mean-squire value of the intensity fluctuations was only 13.7 dB [32]. In their results, the noise level of PA signal is high. Additional noise may be introduced during modulation and demodulation. Attempts have also been made to photoacoustic detection using a low-coherence interferometer [30,51,52]. However, the sensitivity of the low-coherence interferometer decreases with the increase of optical path length difference (OPLD). To address this problem, Lu et al. present a PAI system using a homodyne interferometer with a long coherence length laser that allows for a constant high sensitivity in a large dynamic range of the OPLD [31]. The system locks at the maximum sensitivity during data acquisition. However, this reduces the imaging speed. In this paper, we improved the imaging speed of our previous system and integrated it with OCTA to achieve dual-modal imaging. Recently, a new technique named deep photoacoustic remote sensing (dPARS) has been proposed. Instead of measuring the sample surface displacement in heterodyne and homodyne methods, dPARS detects PA initial pressures by measuring the intensity reflectivity modulations of a low-coherence probe beam [53,54]. dPARS needs Z-scan to image structures at different depth. Besides this, it has many advantages, such as a higher SNR and deeper penetration depth. dPARS may offer new opportunities for clinical translation.

5. Conclusion

In summary, we presented a dual-modal optical system integrating non-contact PAI and OCT. PA signals were acquired using a fiber-based homodyne interferometer. The PA excitation, PA probing and SDOCT probing beams were combined using two dichroic mirrors. Three beams shared the same X-Y galvanometer scanner to perform fast two-dimensional scanning. The PAI acquisition speed was improved by the application of sensitivity compensation and reference arm modulation. PAI and OCTA were performed on the mouse pinna with and without flowing blood. The results indicate that the proposed system is capable of revealing blood flow states in vessels and is useful for the study of diseases associated with blood supply.

Funding

Disclosures

The authors declare that there are no conflicts of interest related to this article.

References

1. P. Carmeliet and R. K. Jain, "Angiogenesis in cancer and other diseases," Nature **407**(6801), 249–257 (2000).
2. P. Carmeliet and D. Collen, "Molecular analysis of blood vessel formation and disease," Am. J. Physiol. **273**(5), H2091–H2104 (1997).
3. L. Pascarella, G. W. Schönbein, and J. J. Bergan, "Microcirculation and venous ulcers: a review," Ann. Vasc. Surg. **19**(6), 921–927 (2005).
4. D. L. Crandall, G. J. Hausman, and J. G. Kral, "A review of the microcirculation of adipose tissue: anatomic, metabolic, and angiogenic perspectives," Microcirculation **4**(2), 211–232 (1997).
5. D. De Backer, J. Creteur, J. C. Preiser, M. J. Dubois, and J. L. Vincent, "Microvascular blood flow is altered in patients with sepsis," Am. J. Respir. Crit. Care Med. **166**(1), 98–104 (2002).
6. Y. Jia, M. R. Grafe, A. Gruber, N. J. Alkayed, and R. K. Wang, "In vivo optical imaging of revascularization after brain trauma in mice," Microvasc. Res. **81**(1), 73–80 (2011).
7. K. M. Poole, D. R. McCormack, C. A. Patil, C. L. Duvall, and M. C. Skala, "Quantifying the vascular response to ischemia with speckle variance optical coherence tomography," Biomed. Opt. Express **5**(12), 4118–4130 (2014).
8. C. A. Park, C. K. Kang, Y. B. Kim, and Z. H. Cho, "Advances in MR angiography with 7T MRI: From microvascular imaging to functional angiography," Neuroimage **168**, 269–278 (2018).
9. D. M. McDonald and P. L. Choyke, "Imaging of angiogenesis: from microscope to clinic," Nat. Med. **9**(6), 713–725 (2003).
10. S. Bash, J. P. Villablanca, R. Jahan, G. Duckwiler, M. Tillis, C. Kidwell, J. Saver, and J. Sayre, "Intracranial vascular stenosis and occlusive disease: evaluation with CT angiography, MR angiography, and digital subtraction angiography," AJNR Am. J. Neuroradiol. **26**(5), 1012–1021 (2005).
11. D. Huang, E. A. Swanson, C. P. Lin, J. S. Schuman, W. G. Stinson, W. Chang, M. R. Hee, T. Flotte, K. Gregory, C. A. Puliafito, and et, "Optical coherence tomography," Science **254**(5035), 1178–1181 (1991).
12. R. K. Wang, "Three-dimensional optical micro-angiography maps directional blood perfusion deep within microcirculation tissue beds in vivo," Phys. Med. Biol. **52**(23), N531–N537 (2007).
13. U. Baran, E. Swanson, J. E. Sanders, and R. K. Wang, "OCT-based microangiography for reactive hyperaemia assessment within residual limb skin of people with lower limb loss," Skin Res. Technol. **24**(1), 152–155 (2018).
14. G. L. Su, D. M. Baughman, Q. Zhang, K. Rezaei, A. Y. Lee, and C. S. Lee, "Comparison of retina specialist preferences regarding spectral-domain and swept-source optical coherence tomography angiography," Clin. Ophthalmol. **11**, 889–895 (2017).
15. L. V. Wang, "Multiscale photoacoustic microscopy and computed tomography," Nat. Photonics **3**(9), 503–509 (2009).
16. T. Liu, Q. Wei, J. Wang, S. Jiao, and H. F. Zhang, "Combined photoacoustic microscopy and optical coherence tomography can measure metabolic rate of oxygen," Biomed. Opt. Express **2**(5), 1359–1365 (2011).
17. Y. Yang, X. Li, T. Wang, P. D. Kumavor, A. Aguirre, K. K. Shung, Q. Zhou, M. Sanders, M. Brewer, and Q. Zhu, "Integrated optical coherence tomography, ultrasound and photoacoustic imaging for ovarian tissue characterization," Biomed. Opt. Express **2**(9), 2551–2561 (2011).
18. L. Li, K. Maslov, G. Ku, and L. V. Wang, "Three-dimensional combined photoacoustic and optical coherence microscopy for in vivo microcirculation studies," Opt. Express **17**(19), 16450–16455 (2009).
19. M. Jeon and C. Kim, "Multimodal photoacoustic tomography," IEEE Trans. Multimed. **15**(5), 975–982 (2013).
20. C. Lee, S. Han, S. Kim, M. Jeon, M. Y. Jeon, C. Kim, and J. Kim, "Combined photoacoustic and optical coherence tomography using a single near-infrared supercontinuum laser source," Appl. Opt. **52**(9), 1824–1828 (2013).

21. S. Jiao, Z. Xie, H. F. Zhang, and C. A. Puliafito, "Simultaneous multimodal imaging with integrated photoacoustic microscopy and optical coherence tomography," Opt. Lett. **34**(19), 2961–2963 (2009).

22. M. Liu, B. Maurer, B. Hermann, B. Zabihian, M. G. Sandrian, A. Unterhuber, B. Baumann, E. Z. Zhang, P. C. Beard, W. J. Weninger, and W. Drexler, "Dual modality optical coherence and whole-body photoacoustic tomography imaging of chick embryos in multiple development stages," Biomed. Opt. Express **5**(9), 3150–3159 (2014).

23. S. A. Carp and V. Venugopalan, "Optoacoustic imaging based on the interferometric measurement of surface displacement," J. Biomed. Opt. **12**(6), 064001 (2007).

24. S. A. Carp, A. Guerra III, S. Q. Duque, Jr., and V. Venugopalan, "Optoacoustic imaging using interferometric measurement of surface displacement," Appl. Phys. Lett. **85**(23), 5772–5774 (2004).

25. A. Hochreiner, J. Bauer-Marschallinger, P. Burgholzer, B. Jakoby, and T. Berer, "Non-contact photoacoustic imaging using a fiber based interferometer with optical amplification," Biomed. Opt. Express **4**(11), 2322–2331 (2013).

26. G. Rousseau, A. Blouin, and J. P. Monchalin, "Non-contact photoacoustic tomography and ultrasonography for tissue imaging," Biomed. Opt. Express **3**(1), 16–25 (2012).

27. P. C. Beard, F. Perennes, and T. N. Mills, "Transduction mechanisms of the Fabry-Perot polymer film sensing concept for wideband ultrasound detection," IEEE Trans. Ultrason. Ferroelectr. Freq. Control **46**(6), 1575–1582 (1999).

28. E. Zhang, J. Laufer, and P. Beard, "Backward-mode multiwavelength photoacoustic scanner using a planar Fabry-Perot polymer film ultrasound sensor for high-resolution three-dimensional imaging of biological tissues," Appl. Opt. **47**(4), 561–577 (2008).

29. M. Liu, Z. Chen, E. Rank, B. Zabihian, E. Z. Zhang, P.C. Beard, H. Kittler, and W. Drexler, "Combined multimodal photoacoustic tomography, optical coherence tomography (OCT) and OCT based angiography system for in vivo imaging of multiple skin disorders in human (Conference Presentation)," SPIE BiOS, 100370T (2017).

30. Y. Wang, C. Li, and R. K. Wang, "Noncontact photoacoustic imaging achieved by using a low-coherence interferometer as the acoustic detector," Opt. Lett. **36**(20), 3975–3977 (2011).

31. J. Lu, Y. Gao, Z. Ma, H. Zhou, R. K. Wang, and Y. Wang, "In vivo photoacoustic imaging of blood vessels using a homodyne interferometer with zero-crossing triggering," J. Biomed. Opt. **22**(3), 036002 (2017).

32. S. J. Park, J. Eom, Y. H. Kim, C. S. Lee, and B. H. Lee, "Noncontact photoacoustic imaging based on all-fiber heterodyne interferometer," Opt. Lett. **39**(16), 4903–4906 (2014).

33. Z. Chen, S. Yang, and D. Xing, "Optically integrated trimodality imaging system: combined all-optical photoacoustic microscopy, optical coherence tomography, and fluorescence imaging," Opt. Lett. **41**(7), 1636–1639 (2016).

34. R. K. Wang, S. L. Jacques, Z. Ma, S. Hurst, S. R. Hanson, and A. Gruber, "Three dimensional optical angiography," Opt. Express **15**(7), 4083–4097 (2007).

35. L. An, T. T. Shen, and R. K. Wang, "Using ultrahigh sensitive optical microangiography to achieve comprehensive depth resolved microvasculature mapping for human retina," J. Biomed. Opt. **16**(10), 106013 (2011).

36. V. J. Srinivasan, S. Sakadžić, I. Gorczynska, S. Ruvinskaya, W. Wu, J. G. Fujimoto, and D. A. Boas, "Quantitative cerebral blood flow with optical coherence tomography," Opt. Express **18**(3), 2477–2494 (2010).

37. I. Grulkowski, I. Gorczynska, M. Szkulmowski, D. Szlag, A. Szkulmowska, R. A. Leitgeb, A. Kowalczyk, and M. Wojtkowski, "Scanning protocols dedicated to smart velocity ranging in spectral OCT," Opt. Express **17**(26), 23736–23754 (2009).

38. D. Royer and E. Dieulesaint, *Elastic Waves in Solids I: Freeand Guided Propagation* (Springer, 2000).

39. L. Lipiainen, K. Kokkonen, and M. Kaivola, "Phase sensitive absolute amplitude detection of surface vibrations using homodyne interferometry without active stabilization," J. Appl. Phys. **108**(11), 114510 (2010).

40. F. Lärmer, A. Schilp, K. Funk, and C. Burrer, "Experimental characterization of dynamic micromechanical transducers," J. Micromech. Microeng. **6**(1), 177–186 (1996).

41. R. G. White and D. C. Emmony, "Active feedback stabilisation of a michelson interferometer using a flexure element," J. Phys. E Sci. Instrum. **18**(18), 658–663 (1985).

42. Z. Ma, Z. He, S. Wang, M. Li, Q. Wang, J. Lv, F. Wang, and Y. Wang, "Practical approach for dispersion compensation in spectral-domain optical coherence tomography," Opt. Eng. **51**(6), 063203 (2012).

43. K. Maslov, H. F. Zhang, S. Hu, and L. V. Wang, "Optical-resolution photoacoustic microscopy for in vivo imaging of single capillaries," Opt. Lett. **33**(9), 929–931 (2008).

44. X. Xu, H. Liu, and L. V. Wang, "Time-reversed ultrasonically encoded optical focusing into scattering media," Nat. Photonics **5**(3), 154–157 (2011).

45. L. V. Wang and H. I. Wu, *Biomedical Optics: Principles and Imaging* (John Wiley & Sons, 2012).

46. S. L. Jacques, "Optical properties of biological tissues: a review," Phys. Med. Biol. **58**(11), R37–R61 (2013).

47. S. Hu, K. Maslov, and L. V. Wang, "Second-generation optical-resolution photoacoustic microscopy with improved sensitivity and speed," Opt. Lett. **36**(7), 1134–1136 (2011).

48. R. J. Thomas, B. A. Rockwell, W. J. Marshall, R. C. Aldrich, S. A. Zimmerman, and R. J. Rockwell, Jr., "A procedure for multiple-pulse maximum permissible exposure determination under the Z136. 1-2000 American National Standard for Safe Use of Lasers," J. Laser Appl. **13**(4), 134–140 (2001).

49. G. Rousseau, B. Gauthier, A. Blouin, and J. P. Monchalin, "Non-contact biomedical photoacoustic and ultrasound imaging," J. Biomed. Opt. **17**(6), 061217 (2012).

50. J. Eom, S. J. Park, and B. H. Lee, "Noncontact photoacoustic tomography of in vivo chicken chorioallantoic membrane based on all-fiber heterodyne interferometry," J. Biomed. Opt. **20**(10), 106007 (2015).
51. Z. Chen, S. Yang, Y. Wang, and D. Xing, "All-optically integrated photo-acoustic microscopy and optical coherence tomography based on a single Michelson detector," Opt. Lett. **40**(12), 2838–2841 (2015).
52. Z. Chen, S. Yang, Y. Wang, and D. Xing, "Noncontact broadband all-optical photoacoustic microscopy based on a low-coherence interferometer," Appl. Phys. Lett. **106**(4), 043701 (2015).
53. P. Hajireza, W. Shi, K. Bell, R. J. Paproski, and R. J. Zemp, "Non-interferometric photoacoustic remote sensing microscopy," Light Sci. Appl. **6**(6), e16278 (2017).
54. P. H. Reza, K. Bell, W. Shi, J. Shapiro, and R. J. Zemp, "Deep non-contact photoacoustic initial pressure imaging," Optica **5**(7), 814–820 (2018).